Seismic and hydroacoustic observations from recent underwater events in the South Atlantic Ocean

Ross Heyburn, David Bowers and David N. Green [ORCID]

AWE Blacknest, Brimpton Common, Reading, RG 7 4RS, U.K. E-mail: ross@blacknest.gov.uk

SUMMARY
To study the location and characterize two underwater events in the South Atlantic Ocean, we analyse both seismic and hydroacoustic signals. The first event (2017 November 15) occurred around 550 km east of Argentina, near the last reported position of the Argentine Navy submarine the ARA San Juan, the seafloor wreck of which was found one year later. The second event (2017 December 1) was due to an aircraft-dropped depth charge, detonated as part of the search for the ARA San Juan. We use signal arrival times and azimuths recorded at two seismic and two hydroacoustic stations to estimate epicentres for both events; our estimates were within 10 km of the ground-truth locations. We used geophysical models and databases to determine the sound-speed structure of the water and the presence of sea-ice to help interpret differences in the frequency content and dispersion of signals at the two hydrophone stations. Hydrophone signals for the 2017 November 15 event contain significant energy at high frequencies, which is inconsistent with an earthquake source. Hydrophone signals for the 2017 December 1 event show frequency modulations consistent with those expected from the known depth and explosive energy. Hydrophone signals from the 2017 November 15 event also show frequency modulations, though differences between these for the two events suggest differences in the details of the source mechanisms. Using estimates of the local seismic magnitudes, the peak pressures recorded on the hydrophones, and the known charge weight for the 2017 December 1 event, we estimate that the 2017 November 15 event had an acoustic energy release equivalent to around 428 kg of trinitrotoluene. This analysis demonstrates the importance of high-precision traveltime predictions from models of seismic and ocean acoustic velocities when analysing low-magnitude underwater events.

Key words: Atlantic Ocean; Acoustic properties; Earthquake monitoring and test-ban treaty verification; Wave propagation.

1 INTRODUCTION

On 2017 November 15, during a routine patrol in the South Atlantic Ocean, contact was lost with the Argentine Navy submarine the ARA San Juan. Various media outlets, including the British Broadcasting Corporation (British Broadcasting Corporation 2017), reported the position of the last known point of contact with the ARA San Juan to be around 500 km east of Argentina (Fig. 1a). On 2017 November 23, the Comprehensive Nuclear-Test-Ban Treaty Organisation (CTBTO) published a media advisory (CTBTO 2017) noting that signals from an underwater impulsive event that occurred at 1351 UTC on 2017 November 15 in the vicinity of the last known position of the missing ARA San Juan had been detected at two International Monitoring System (IMS) hydroacoustic stations (at the Crozet Islands and Ascension Island). Several days later, event information was published in the Reviewed Event Bulletin (REB) produced by the International Data Centre (IDC).

The hydroacoustic part of the IMS network, which consists of six hydrophone stations and five *T*-phase stations, is designed to detect underwater nuclear test explosions wherever they might occur in the oceans. Underwater explosions generate acoustic signals, and with the efficiency of underwater acoustic propagation (Jensen *et al.* 2000), these signals which are often referred to as *H*-phases can be detected at long distances. The IMS hydroacoustic network can therefore be used to study events with magnitudes much lower than those expected for an underground nuclear test explosion. For example, Prior & Brown (2010) have shown that signals from a series of underwater explosions with trinitrotoluene (TNT) equivalent charge weights of 34 kg located east of Japan could be detected at an IMS hydrophone station 16300 km away off the coast of Chile. Increasingly data from the IMS network of hydrophone stations are also being used to study a diverse range of natural sources. These studies include monitoring drifting icebergs (Evers *et al.* 2013), studying the vocalization of whales (Le Bras
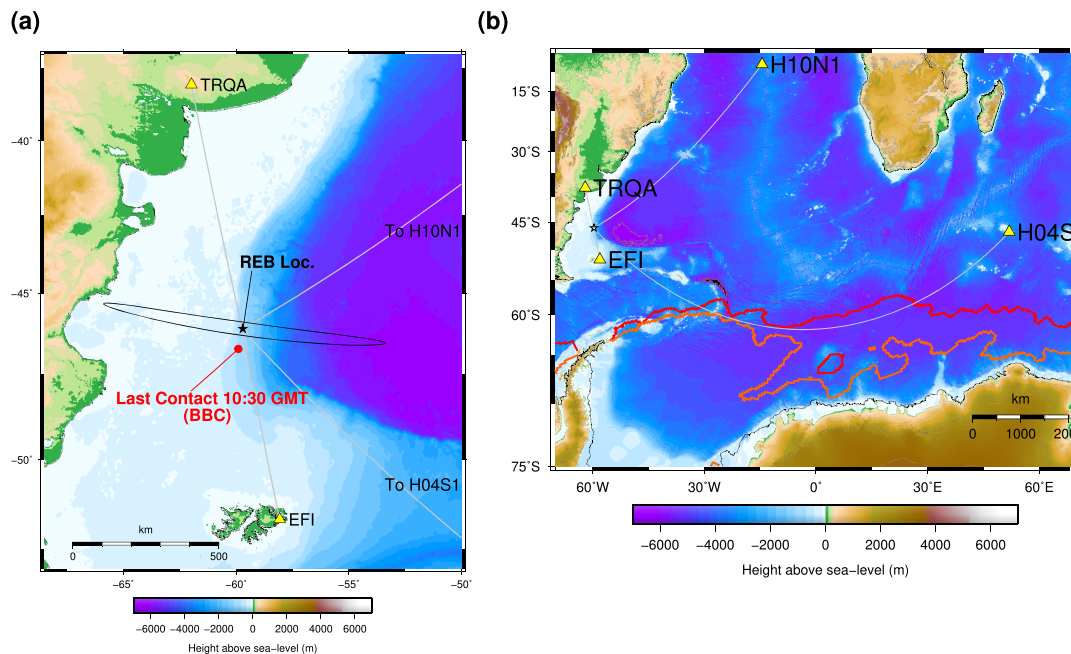
Figure 1. (a) Location map showing the REB epicentre and uncertainty ellipse for 171115. Great-circle paths from the REB epicentre to the stations are also displayed along with the last known position of the ARA San Juan submarine reported by the media. (b) Location map showing the locations of hydroacoustic and seismic stations that recorded signals from 171115. The red and orange lines mark the extent of the area around Antarctica covered by sea ice at greater than 15 percent mean concentration in the months of November 2017 and December 2017.

et al. 2016) and tracking submarine volcanic activity (Metz *et al.* 2018).

As well as hydroacoustic signals, underwater explosions can also generate signals that can be detected by seismic sensors on land. Signals recorded on the large global network of seismic sensors including those that are part of the IMS, can therefore be useful for detecting and characterizing underwater events. Acoustic pressure waves in the water convert to seismic waves on the seafloor and seismic phases can be detected at seismometer stations that are long distances from the coast. For example, Heyburn *et al.* (2018) showed how seismic signals could be used to characterize US Navy shock trial explosions off the east coast of Florida and Baumgardt & Der (1998) showed how the spectra and cepstra of seismic waves from a series of underwater explosions in the Gulf of Bothnia and the Baltic Sea can be used to characterize explosion sources. Data from the global network of seismic sensors have also in the past been used to detect, locate and characterize signals generated as a result of a submarine disaster. Two events associated with the sinking of the Russian Navy submarine APL Kursk on 2000 August 12 generated seismic signals that were recorded at stations in Scandinavia (Koper *et al.* 2001). These signals were used to locate and characterize the two events (e.g. Koper *et al.* 2001; Savage & Helmberger 2001; Bowers & Selby 2009) and help understand the causes of the Kursk submarine disaster.

In this study, seismic and hydroacoustic data are analysed from the 2017 November 15 event (henceforth 171115) that occurred near the last known point of contact with the ARA San Juan submarine. One of the principal motivations of the study was to obtain a good estimate of the location of 171115 to provide support to the search and rescue operations that were conducted after the ARA San Juan went missing. Other studies estimated an epicentre for 171115 using hydroacoustic signals only (Dall'Osto 2019; Vergoz *et al.* 2019) and

Table 1. Source parameters provided by the United Kingdom Royal Navy (personal communication 2017) for 171201.

Parameter	Value
Charge weight	113 kg (250 lbs)
Date	2017 December 1
Time	2004 UTC
Aircraft location at time of drop	45.67°S, 59.42°W
Speed of aircraft	180 knots
Altitude of aircraft	152 m (500 feet)
Course of aircraft	120°
Expected depth of detonation	46 m (150 feet)

also by combining seismic and hydroacoustic data (Nielsen *et al.* 2020). In this study, we examine the importance of traveltime predictions from high precision geophysical models when estimating the location of 171115 using observations from a small number of Global Seismographic Network (GSN) seismometer stations and IMS hydroacoustic stations.

The wreck of the ARA San Juan was eventually found on 2018 November 17 in a search carried out using seabed exploration equipment deployed from Ocean Infinity's Seabed Constructor vessel (Ocean Infinity 2018). Prior to the discovery of the wreck, ground-truth data from a depth charge which was dropped from an Argentine Navy aircraft as part of a calibration experiment and detonated underwater on 2017 December 1 (henceforth 171201) close to the presumed location of 171115 provided an opportunity to validate the approach developed in this study. As the source of 171201 is an underwater explosion with a known charge weight and detonation depth (event details in Table 1), the data from this event are also helpful for testing the location method and characterizing signals recorded from 171115.

2 HYDROACOUSTIC DATA

H-phase detections were reported by the IDC at triplets of hydrophone sensors located at the H10 hydrophone station at the Ascension Island and the H04 hydrophone station at the Crozet Islands (locations in Fig. 1b) for both 171115 and 171201. Fig. 2(a) displays waveforms with the instrument response removed for hydrophone sensors H10N1 and H04S1 for 171115. Fig. 2(a) shows that the signals at H10N1 contains energy at frequencies up to 80 Hz. The presence of significant energy at high frequencies means the source is unlikely to be an earthquake, as signals generated by undersea earthquakes contain predominantly low-frequency energy (Okal 2001). At H04S1, the signals are not seen above the background noise level at frequencies above 40 Hz and the signal duration is longer than observed at H10N1.

Fig. 2(b) displays the waveforms recorded on H10N1 and H04S1 for 171201. As for 171115, at H10N1 the signals contain significant energy at high frequencies. At both H10N1 and H04S1, at frequencies less than around 40 Hz, the maximum positive recorded pressures are larger for 171115 than 171201. At frequencies above 40 Hz, the maximum positive recorded pressures are larger for 171201 than 171115, and in the 40 to 60 Hz passband signals from 171201 are clearly observed whilst they were not for 171115. As for 171115, the 171201 signal durations are longer at H04S1 than H10N1.

At H10N1, Fig. 2(a) shows that a second and third group of signals of lower amplitude are also observed around 100 and then 150 s after the initial *H*-phase arrival. These later arriving signals which are not observed at H04S1 have been interpreted as reflections and refractions from topographic features in the Atlantic Ocean (Dall'Osto 2019; Vergoz *et al.* 2019; Nielsen *et al.* 2020). The presence of these later arriving signals in the waveforms from 171201 in Fig. 2(b) is evidence that these signals are a result of the propagation path and are not a source effect.

Figs 2(a) and (b) show that the signals filtered in different passbands from both 171115 and 171201 at H04S1 have either lower signal-to-noise ratios (SNRs) or are not observed at high frequencies, and are longer duration and more dispersed than the corresponding waveforms recorded by H10N1. In the Southern Ocean, there is a significant change in shallow water temperature on either side of the boundary of the Antarctic Circumpolar Current (ACC) which flows eastward around Antarctica (Nowlin & Klinck 1986). This boundary separates cold water to the south from warmer subtropical waters to the north and typically occurs at latitudes of between 50°S and 60°S. South of this boundary, the axis of the Sound Fixing and Ranging (SOFAR) channel, which is typically 100–1000 m deep in subtropical waters, disappears as the overlaying higher velocity layer thins to nothing. A significant portion of the propagation path from 171115 and 171201 to H04S1 is at latitudes to the south of the ACC boundary (Fig. 1b). de Groot-Hedlin *et al.* (2009) showed that group velocities for different acoustic modes have a wider range when propagating in the ACC than at mid-latitudes. This can result in signals with greater dispersion and hence longer durations for source-to-station propagation paths which have significant portions in the ACC. Another environmental factor to consider at latitudes south of the ACC boundary is the presence of sea ice at the sea surface. When acoustic waves interact with rough sea ice, it has a significant impact on signal attenuation with signal propagation amplitude loss increasing rapidly with frequency due to scattering (Gavrilov & Mikhalevsky 2006).

To investigate these effects further, sound-speed profiles for the paths from the REB epicentre for 171115 to H10N1 and H04S1 were derived using seasonal climatological data from the 2009 World Ocean Atlas (Antonov *et al.* 2010; Locarnini *et al.* 2010). Fig. 3(a) shows that for the path from 171115 to H10N1, there is a well-defined SOFAR channel at depths between 250 and 1000 m which is bounded by an overlying higher velocity layer. For the path from 171115 to H04S1, Fig. 3(b) shows that for a large portion of the propagation path, the axis of the SOFAR channel is at the surface and there is no overlying higher velocity layer.

The ray paths of hydroacoustic waves from the REB epicentre for 171115 to H10N1 and H04S1 have been calculated using the BELLHOP Gaussian beam ray tracing methodology (Porter & Bucker 1987). Sound speed profiles at 1000 km intervals along the path were extracted from the 2009 World Ocean Atlas (Figs 3a and b) and were used to provide a range dependent sound speed model for the ray tracing. The results of a simulation where 36 acoustic rays were launched from the source at a depth of 90 m in the water at angles between −89° and 89° towards H10N1 and H04S1 are shown for selected portions of the propagation paths in Figs 3(c) and (d).

The propagation paths from 171115 to H10N1 and H04S1 are not completely clear of bathymetric blockages which project at least part of the way into the SOFAR channel. Along the path to H10N1, Fig. 3(c) shows that between distances of 2600 km and 2850 km, sound wave propagation is bounded by the sea surface and the Rio Grande Rise. For the path to H04S1, Fig. 3(d) shows there is a bathymetric blockage which interferes with sound propagation between distances of 2550 km and 2700 km (South Sandwich Island Arc). Away from these topographic features, Fig. 3(c) shows that for the path to H10N1, sound wave propagation is bounded by the overlying higher velocity layer. In contrast, for the path to H04S1, Fig. 3(d) shows that sound wave propagation is bounded by the sea surface because of the absence of the overlying higher velocity layer. The different sound speed profiles along the source-to-station paths are therefore a potential explanation for the differences in signal durations between the signals observed at H10N1 and H04S1.

Given that sound wave propagation is bounded by the sea surface for the path to H04S1, data on the extent of sea ice were extracted from the National Snow and Ice Data Center database (Fetterer *et al.* 2017). Fig. 1(b) shows the extent of the area around Antarctica covered by sea ice at greater than 15 per cent mean concentration in the months of November and December 2017. A significant portion of the path to H04S1 in November 2017 is in this area and provides a possible explanation for the absence or low SNRs of signals observed at high frequencies at H04S1 for 171115. Fig. 1(b) also shows that there are changes in the extent of sea ice during the months of November and December which suggests that for 171115 and 171201 signal attenuation along the propagation paths may be different.

3 OBSERVED SEISMIC DATA

The data from the three-component broad-band GSN seismic stations at EFI (East Falkland Island) and TRQA (Tornquist, Argentina) were obtained from the Incorporated Research Institutions for Seismology (IRIS) database for 171115 and 171201. The three components from the borehole instruments (at 80 and 32 m depths at EFI and TRQA respectively) were corrected for the instrument response to recover ground displacement, and oriented to the verti-
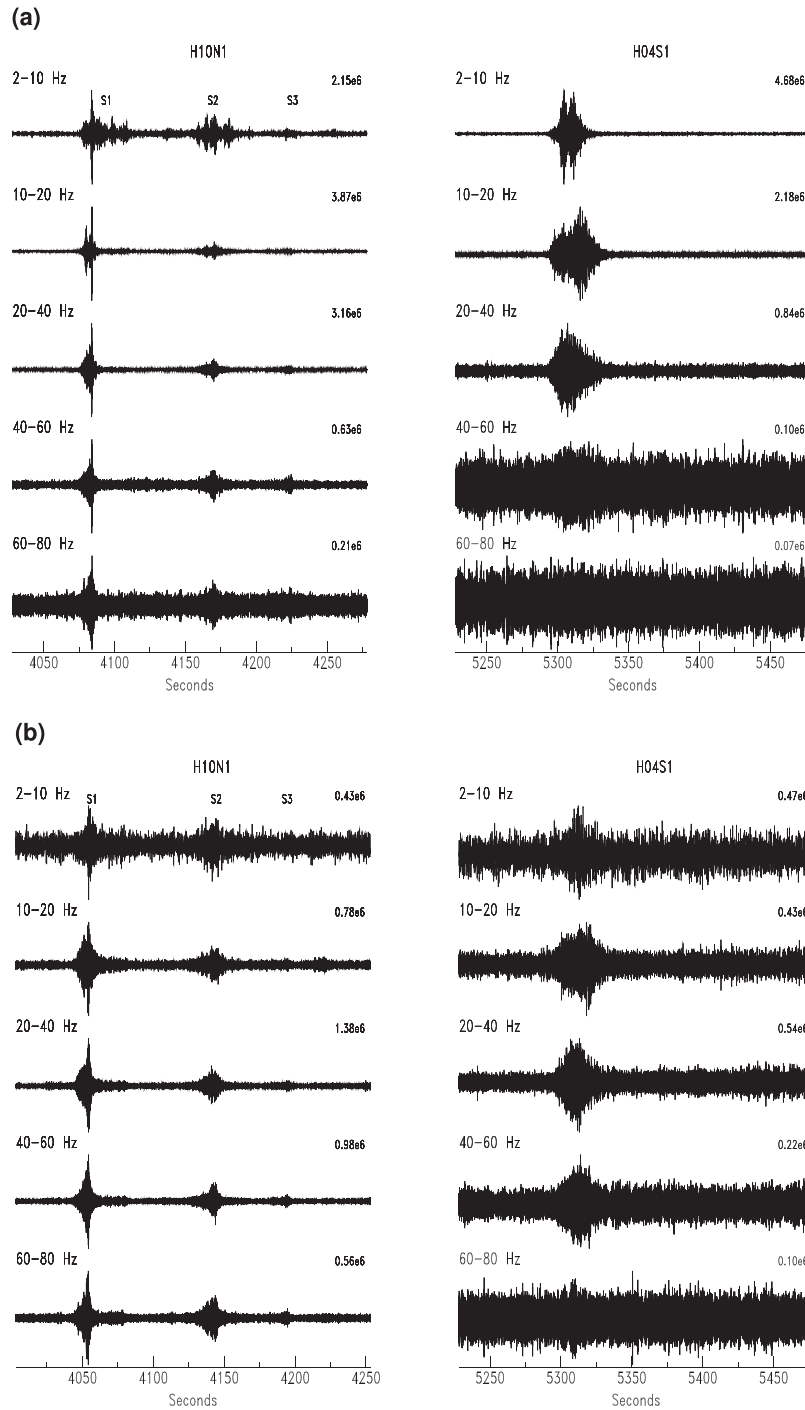
(a)

(b)

Figure 2. (a) Signals observed from 171115 at H10N1 and H04S1. The instrument response has been removed and the signals are displayed for different bandpass filters. The three signals observed at H10N1 are marked as s1, s2 and s3. The time is in seconds after the estimated event origin time. The number to the top right of each trace is the maximum positive pressure in μPa. (b) Signals observed from 171201 at H10N1 and H04S1.

cal (Z), radial (R) and tangential (T) components assuming the REB epicentres. The seismograms were interpreted in terms of regional seismic phases, considering the REB epicentres and origin time, and that Pn and Pg energy is more likely on the Z and R components, and Sn energy can be on all three (Kennett 1993). Figs 4(a) and (b) show the waveforms associated with 171115 filtered in the 3.5–7.0 Hz passband, and the regional seismic phase picks made in this study. For 171201, Pn seismic signals were only observed at TRQA (Fig. 5).

To estimate the local magnitudes, M_L^P, for both 171115 and 171201, the local magnitude scale developed by Green (2017) for high-frequency regional P (1.5-30 Hz) from the UK has been used. The original vertical component data were converted to a common instrument response and are bandpass filtered with a passband of 3.5–5.0 Hz. The maximum half peak-to-peak amplitude, A, in a time window which included Pn and Pg, was read by an analyst. Table 2 shows these amplitudes for seismometer stations EFI and TRQA for 171115 along with the distance corrections, $B(\Delta)$, estimated by
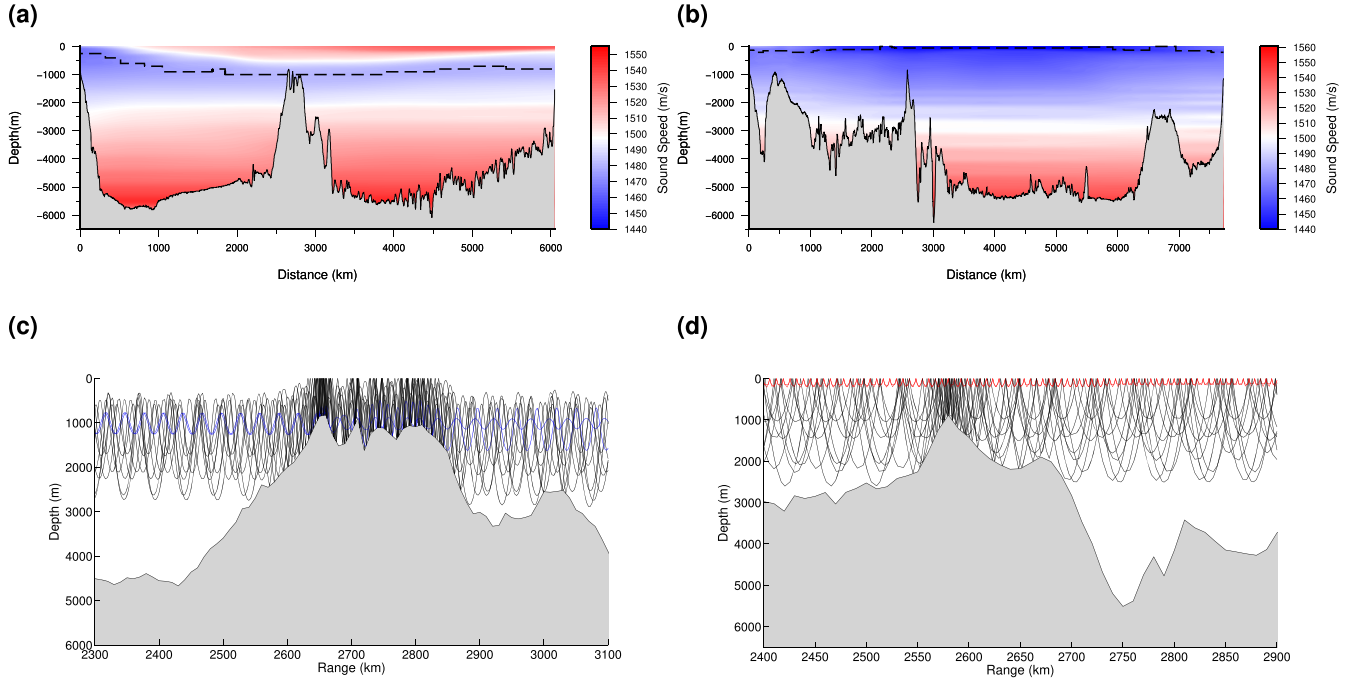
(a) **(b)**

(c) **(d)**

Figure 3. (a) Ocean sound speed profile and bathymetry along the great-circle path from the estimated location of 171115 to the H10N1 hydrophone sensor. The dashed line is the axis of the Sound Fixing and Ranging Channel. (b) Ocean sound speed profile and bathymetry along the great-circle path from the estimated location of 171115 to the H04S1 hydrophone sensor. (c) Ray paths predicted using a BELLHOP (Porter & Bucker 1987) eigenray simulation for a source at 90 m depth. Only the ray paths predicted at distances between 2300 and 3100 km along the path from the location of 171115 to H10N1 are displayed. Rays which only reflect off the seafloor are shown in blue. (d) Ray paths predicted along the path from 171201 to H04S1. Rays which only reflect off the sea surface are shown in red.

Green (2017). Following Green (2017), M_L^P is estimated using the following equation,

$$M_L^P = \log_{10}(A) + B(\Delta) + S, \tag{1}$$

where S is the station effect. As S is unknown for stations EFI and TRQA, it is set to zero. The resulting network average M_L^P from the two seismometer stations EFI and TRQA is 2.05 for 171115. The local magnitude, M_L^P, was also estimated for 171201 using only the data recorded at TRQA. The resulting M_L^P of 1.97 is lower than the M_L^P of 2.38 which was estimated at TRQA for 171115. Table 2 shows the amplitude for seismometer station TRQA along with the distance corrections, $B(\Delta)$, for 171201.

4 LOCATION

The epicentre, depth and origin time of a seismic disturbance can be estimated by minimizing the difference between the observed onset times, azimuths and slownesses of seismic signals, and those predicted by a model of the Earth. Various studies have shown that reliable epicentres of seismic events can be estimated in this way using a few (four to six) seismic stations (Evernden 1969; Jordan & Sverdrup 1981). The inclusion of azimuth measurements from array stations can also help constrain the location of events detected at small numbers of stations (Bratt & Bache 1988).

In this study, the observed times and azimuths of hydroacoustic signals (*H*-phases) are used in combination with the seismic data to help improve the accuracy and precision of the estimated epicentre. At a seismic or hydroacoustic station, i, the onset time, t_i, is given by,

$$t_i = t_0 + T(\Delta_i, h) + S_i + \epsilon_i, \tag{2}$$

where t_0 is the origin time, $T(\Delta_i, h)$ is the traveltime predicted though an Earth or Ocean model at source-station distance Δ_i and for source depth h, S_i is a station path correction to the model which may or may not be known, and ϵ_i is the residual error, usually attributed to measurement error. In the usual case, S_i and ϵ_i are not known, and are modelled as normally distributed uncorrelated random variables, with variance σ^2. The uncertainty in the arrival time, σ, is then given by

$$\sigma^2 = \sigma_s^2 + \sigma_e^2, \tag{3}$$

where σ_e is the reading error and σ_s is the model error. The location itself is estimated by iteratively minimizing the sum of squared weighted residuals between the observed and predicted traveltimes and azimuths.

As the location of 171201 was known, prior to the discovery of the wreck of the ARA San Juan, this provided a useful validation of the approach taken in this study. For 171201, for a fixed source depth of 0 km, the remaining hypocentre parameters (epicentre and origin time) of 171201 are determined using arrival times and azimuths of *H*-phases published in the REB for H04S1 and H10N1, and the P_n arrival time picked at the three-component seismic station TRQA (Argentina). These values are shown in Table 3.

The IASPEI 1991 traveltime tables are used to calculate predicted seismic arrival times, and for the regional seismic phases the Regional Seismic Travel Time (RSTT; Myers *et al.* 2010) corrections from the 2014 RSTT 3-D model (rstt201404um) were applied. For the *H*-phases, traveltimes were predicted using a constant H speed of 1.485 km s^{-1} with a correction derived from monthly 2-D radial traveltime corrections and model uncertainty, σ_s^2. The 2-D radial traveltime corrections used here are the same as those used by the IDC and these are calculated using the KRAKEN normal-mode
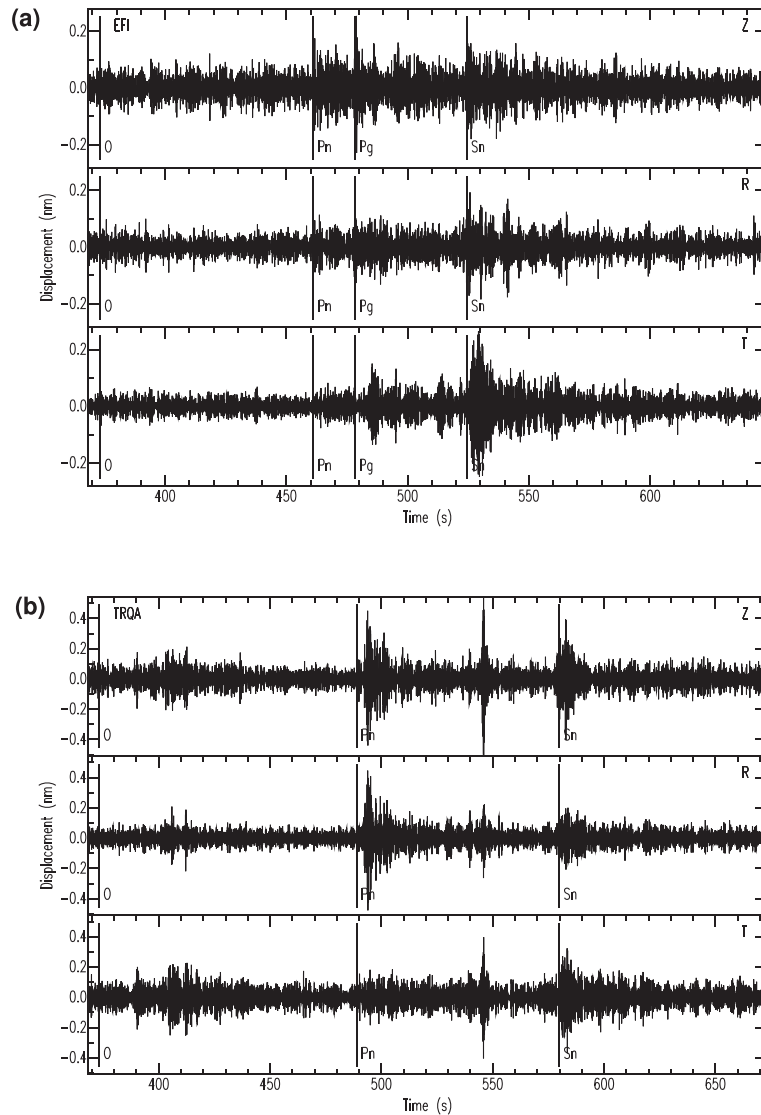
Figure 4. Three-component seismic data recorded for 171115. The data are ground displacement (in nm) filtered 3.5–7.0 Hz, and oriented as vertical, radial and tangential components of motion (traces from top to bottom). The onset time picks from this study for Pn, Pg, and Sn are also shown. The REB origin time is marked by 'O'. Only Pn onset times were used for the epicentres estimated in this study. (a) Data from the seismic station at EFI (East Falkland Island). (b) Data from the seismic station at TRQA (Argentina).

acoustic propagation model using data from bathymetry, sea water sound-speed and sediment thickness databases (Prior 2009). As 171201 was at the start of the December, the mean of the traveltime corrections for November and December was used for this event. Predicted H-phase traveltime corrections can be large, 10.9 and 78.8 s for H10N1 and H04S1 respectively for 171201.

For the seismic regional phases the reading error σ_e is a nominal value based on our experience, the SNR, and how emergent the signal onset appears. The model error, σ_s, is from the RSTT model. For the H-phase arrival times, σ_e is nominal and based on the duration of the H-phase signal envelope. Larger values of σ_e were therefore used in this study for H-phases observed at H04S1 than for those observed at H10N1 as a result of the longer duration of the observed H-phases (see Tables 3 and 4). σ_e used for the H-phase azimuths are from the IDC database.

The resulting hypocentre parameters and associated uncertainty (coverage) ellipses (at 90 per cent level) for 171201 are shown in Table 5 and displayed in Fig. 6(a). The epicentre estimated using

this approach for 171201 is around 10 km south of the location at which the depth charge 171201 was dropped from the aircraft and is within the estimated uncertainty ellipse. The parameters, corrections and velocity models used to estimate the epicentre of 171201 were therefore presumed to be reasonable which provided confidence that a similar approach could be taken to estimate the location of 171115 prior to the discovery of the wreck. For 171115, the P_n arrival time picked at the three-component seismic station EFI was used in addition to arrival time and azimuth information from stations H04S1, H10N1 and TRQA (see Table 4 for details). The epicentre estimated for 171115 using this approach is around 10 km southwest of the location of the wreck and is within the estimated uncertainty ellipse (Fig. 6a). Epicentres estimated for 171115 and 171201 without the 2-D and 3-D radial traveltime corrections for the H-phases and the RSTT corrections for the seismic phases are shown in Fig. 6(b). These estimated epicentres were 72 km from the wreck location and 94 km from the location at which the depth charge 171201 was dropped from the aircraft which emphasizes
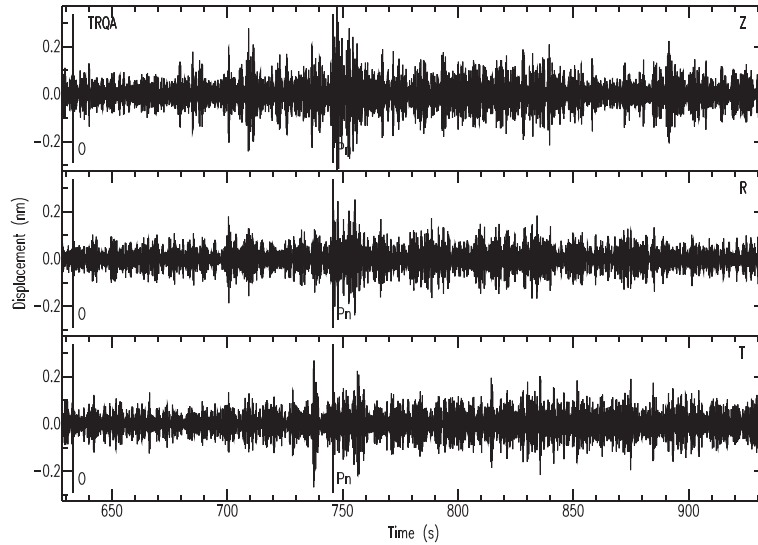
Figure 5. Data from the three-component seismic station at TRQA (Argentina) for 171201. The data are ground displacement (in nm) filtered 3.0–6.0 Hz, and oriented as vertical, radial and tangential components of motion (traces from top to bottom). The onset time pick from this study for Pn is shown. The REB origin time is marked by 'O'.

Table 2. M_L^P observations for 171115 and 171201 estimated using the *P*-wave magnitude scale of Green (2017). Δ, epicentral distance in kilometres; A, displacement amplitude in nm; $B(\Delta)$, distance correction used for M_L^P calculation.

Event	Station	Δ (km)	A (nm)	$B(\Delta)$	M_L^P
171115	EFI	639.9	0.29	2.27	1.73
	TRQA	904.4	0.45	2.72	2.38
Network average					2.05
171201	TRQA	870.3	0.26	2.56	1.97

the importance of the traveltime corrections for obtaining accurate location estimates of small underwater events recorded by only a few stations.

5 SOURCE CHARACTERIZATION

One of the most commonly observed features of the amplitude spectra of *H* phases from underwater explosions is a harmonic series of modulations caused by interference between the primary pulse generated by the explosion and later pulses generated by the oscillating size of the gas bubble created by the explosion. If an explosion does not break the surface of the water, the bubble generated by the explosion expands and contracts in size. As bubbles expand, the hydrostatic pressure eventually confines them and in the resulting contraction and expansion acoustic energy is released. During the contraction of the gas bubble, the gas temperature and pressure increases until expansion occurs again and the cycle is repeated. Recorded signals therefore contain a series of impulses starting with the initial explosion and then followed by signals generated by successive oscillations in bubble size. The frequency of bubble pulse modulations, f_b (in Hz), can be written as (e.g. Chapman 1985)

$$f_b = \frac{(d + 10)^{\frac{5}{6}}}{2.1 W^{\frac{1}{3}}}, \tag{4}$$

where d is the detonation depth (in metres) and W is the TNT equivalent charge weight (in kg) of the explosion.

Information provided by the United Kingdom Royal Navy (Table 1) suggests that 171201 was an Mk 54 depth charge containing approximately 250 lbs (113 kg) of explosives. Here it is assumed that the Mk 54 depth charge used contains the explosive HBX-1 (United States Navy Department 1947). When considering blast effects from explosives, explosive yields are usually defined in terms of equivalency to the explosive TNT. Using a thermomechanical computer code, Maienschein (2002) have calculated TNT equivalencies for various types of explosive with respect to peak pressure. Maienschein (2002) calculate a TNT equivalence of 1.49 for explosive HBX-1 of the type assumed to be used in Mk 54 depth charges (40 per cent RDX, 38 per cent TNT). Assuming 113 kg of HBX-1, the TNT equivalent charge weight of the Mk 54 depth charge is 168 kg. For a TNT equivalent charge weight of 168 kg and a detonation depth of 46 m, eq. (4) predicts a bubble pulse frequency of 2.47 Hz for 171201.

Data recorded at H10N1 and H04S1 have been used to compute amplitude spectra for the recorded *H*-phase signals from 171115 and 171201. Fig. 7(a) shows that a pattern of modulations is seen in the amplitude spectra for 171201 with mean frequency differences between adjacent minima of 2.20 Hz at both H10N1 and H04S1 which is similar to the 2.47 Hz predicted by eq. (4).

A pattern of modulations is also observed in the spectra from 171115, however, there are differences between the spectra observed for the two events. For 171201, Fig. 7(a) shows that the frequency of the minima and maxima are very similar on the spectra recorded at H10N1 and H04S1. However for 171115, the frequency of the minima and maxima in the spectra varies between H10N1 and H04S1. The variations in the mean frequency difference between adjacent minima recorded at H10N1 (2.83 Hz) and H04S1 (3.02 Hz) are not observed from 171201.

As observed from the hydrophone sensor waveforms, Fig. 7(b) shows that at frequencies less than 40 Hz the recorded pressures from 171115 are larger than those from 171201. At frequencies above 40 Hz, the recorded pressures from 171201 are larger than those from 171115. Differences are also observed in the autocorrelation traces calculated for 171115 and 171201 in the 8–64 Hz

Table 3. Arrival times and azimuths used to locate 171201. Δ, epicentral distance in degrees; ϕ, azimuth from source to station; Time/Az., measured arrival time/backazimuth of the signal arriving at the station; σ_e, assumed uncertainty in arrival time/azimuth measurement; σ_s, assumed uncertainty in predicted traveltime (model error).

Station	Phase	Δ (°)	ϕ (°)	Time/Az. (UTC) / (°)	σ_e (s) / (°)	σ_s (s)
TRQA	Pn	7.94	345.191	20:06:25.7	2.00	2.7265
H10N1	H	54.00	59.882	21:12:05.195	1.00	2.611
				216.8	3.40	
H04S1	H	69.85	137.066	21:32:59.876	6.00	12.382
				224.4	3.11	

Table 4. Arrival times and azimuths used to locate 171115. Δ, epicentral distance in degrees; ϕ, azimuth from source to station; Time/Az., measured arrival time/backazimuth of the signal arriving at the station; σ_e, assumed uncertainty in arrival time/azimuth measurement; σ_s, assumed uncertainty in predicted traveltime (model error).

Station	Phase	Δ (°)	ϕ (°)	Time / Az. (UTC) / (°)	σ_e (s) / (°)	σ_s (s)
EFI	Pn	5.75	169.092	13:52:41.2	2.00	1.4589
TRQA	Pn	8.14	347.820	13:53:09.0	2.00	2.7265
H10N1	H	54.38	60.090	14:59:16.878	1.00	2.573
				217.0	2.88	
H04S1	H	69.83	137.205	15:19:37.587	6.00	9.296
				223.5	2.72	

Table 5. Epicentres estimated for 171115 and 171201. Smaj, semi-major axis of 90% coverage ellipse. Smin, semi-minor axis of coverage ellipse. Azi, azimuth of major axis of coverage ellipse.

Event	Latitude (°)	Longitude (°)	Depth (km)	Smaj (km)	Smin (km)	Azi (°)	Origin Time (UTC)
171115	−46.0426	−59.8096	0 (fixed)	27.4	10.5	144.4	13:51:14.357 ± 2.1s
171201	−45.7660	−59.4164	0 (fixed)	40.3	14.4	158.9	20:04:30.858 ± 3.8s

passband with the phase of the delayed wavelet appearing to be different for the two events at H10N1, and the autocorrelation traces generally more complex for 171115 when compared with those recorded for 171201 (Fig. 8). For 171201, the autocorrelation trace shows a clear peak at a delay from the central peak of around 0.45 s (equivalent to a frequency of 2.2 Hz) which is consistent with modulations observed in the spectra at H10N1 and H04S1. The pulse generated by the second bubble oscillation from 171201 can also be seen at around 0.90 s at H04S2 and H04S3.

As the approximate charge weight of 171201 is known, an estimate of the charge weight of TNT that the acoustic energy release from 171115 is equivalent to can be estimated using the difference in magnitude of the observed seismic phases, and the difference in pressures recorded at the H10 hydrophone station for the two events. Using seismic data recorded at TRQA, an M_L^P of 2.38 was calculated for 171115 and 1.97 for 171201. The 0.41 difference in magnitude units (m.u.) corresponds to the source of 171115 being roughly 2.6 times larger than 171201. Pressures measured at H10N1 are also compared for 171115 and 171201. The maximum half peak-to-peak pressure was read from the hydrophone sensor data in the 1 to 100 Hz passband. A maximum half peak-to-peak pressure of 6.25 Pa was measured for 171115 and 2.46 Pa was measured for 171201. These recorded pressures correspond to 171115 being 2.5 times larger than 171201 which is similar to the 2.6 estimated from the seismic data recorded at TRQA. Data from H04S1 were not used as due to the potential effect of variations in the amount of ice present at the sea surface during the Southern Hemisphere spring, attenuation of acoustic waves along the propagation

paths may vary for the two events. A TNT equivalent acoustic energy release of 428 kg has been estimated for 171115 by multiplying the known charge weight for 171201 by 2.55 (the mean value of the two factors estimated from the seismic and hydroacoustic observations). Uncertainty in the depth in the water at which 171115 occurred means that there is uncertainty in this estimate of the energy release. Previous studies have shown that for explosive sources detonated underwater, the detonation depth in the water can have a significant effect on the amplitude of the observed seismic signals (Jacob & Neilson 1977), and the amount of acoustic energy released in the frequency band recorded by IMS hydrophones (Prior & Brown 2010).

6 DISCUSSION AND CONCLUSIONS

Seismic and hydroacoustic data from the IMS and GSN played a vital role in helping to locate the missing submarine ARA San Juan, both in the initial search which took place immediately after the submarine went missing in 2017 and during the search which eventually located the wreck of the submarine in 2018. With signals recorded at only two GSN seismic and two IMS hydrophone stations, to obtain a high precision estimate of the location of 171115, multiple geophysical models helped us to interpret the observed signals and make the accurate seismic and hydroacoustic traveltime predictions required. Results in this study demonstrate the importance of the 2-D radial traveltime corrections for the *H*-phases and the RSTT corrections for the seismic phases. Without these corrections, epicentre estimates for both 171115 and 171201 were over 70 km from
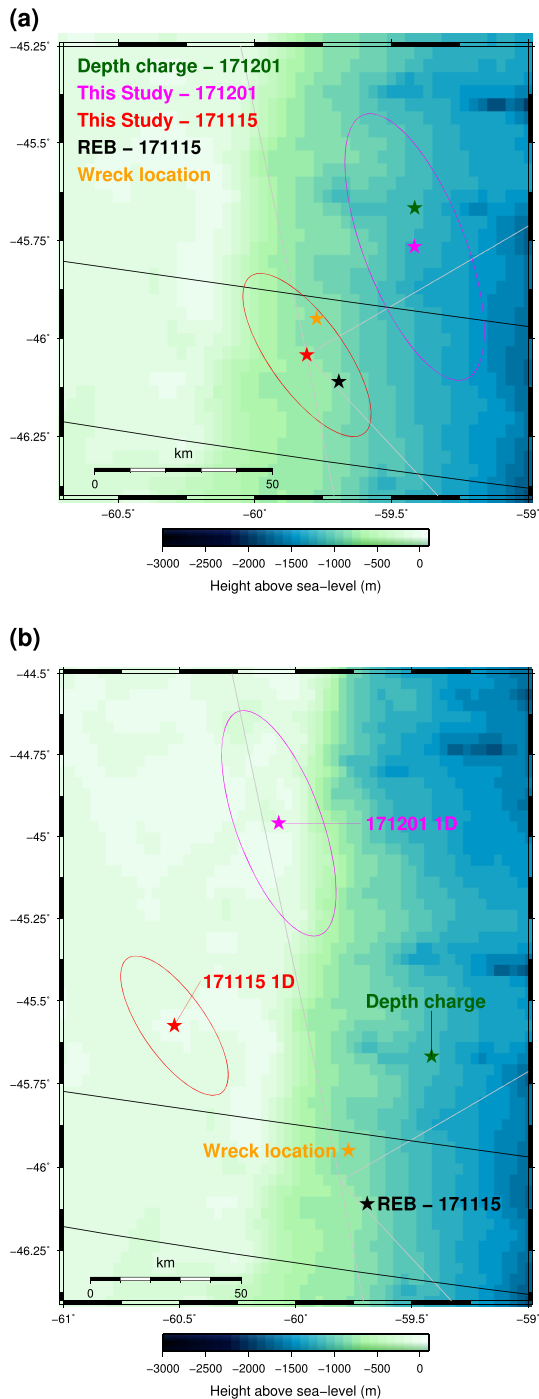
Figure 6. (a) Location map showing epicentres and 90 per cent uncertainty ellipses estimated in this study for 171115 and 171201 using 2-D hydroacoustic traveltime corrections and RSTT corrections. The ground-truth location of 171201 and the location of the wreck found by the Seabed Constructor are also displayed along with the REB epicentre and uncertainty ellipse for 171115. Great-circle paths from the epicentre estimated in this study for 171115 to the stations are also displayed. (b) Location map showing epicentres and 90 per cent uncertainty ellipses estimated without the 2-D hydroacoustic traveltime corrections and RSTT corrections for 171115 and 171201.

the ground-truth locations of both events. When the corrections are applied, the location of 171115 was estimated to within 10 km of the location of the wreck of the ARA San Juan. The location of 171115 was estimated in this study prior to the ARA San Juan being found so the proximity of the location estimate for 171201 to the ground-truth location provided confidence that the approach used was valid during the search.

Geophysical models were also useful for understanding differences in the frequency content and dispersion of hydroacoustic signals observed at the H10 and H04 hydrophone stations from both 171115 and 171201. These hydroacoustic path effects, interpreted as being the result of acoustic wave propagation bounded by the sea surface and the presence of sea ice, could potentially have implications for source identification and location techniques. Explosion sources in the water can be identified based on their spectral characteristics as they generally have a shorter duration and a wider frequency band (Hanson *et al.* 2001) than naturally occurring events such as undersea earthquakes. Differences in transmission loss observed in the 40–80 Hz passband for the paths to the H04 and H10 hydrophone stations means that the effectiveness of methods which rely on these signal characteristics may be path dependent. There may also be a dependence on the time of year due to seasonal variability in both the extent of sea ice and the sound-speed structure of the Ocean. For source location estimates, seismic sources which generate longer duration and more complex waveforms often have larger errors in their measured arrival times (Bóndar *et al.* 2004) which contributes to location uncertainty. The long duration of signals observed at H04S1 suggest that for some source-to-station paths care must be taken when measuring the arrival times of *H*-phases and assigning appropriate reading errors.

Hydroacoustic signals detected for the known depth charge explosion, 171201, displayed the characteristics expected for an underwater explosion and the observed bubble pulse frequency was consistent with the ground-truth data. Despite some similarities in the spectra observed for 171115 and 171201, as discussed in the previous section, the modulations in the spectra from 171115 differ from those observed for 171201, and the autocorrelation traces for 171115 and 171201 are also different. These frequency differences are not consistent with an uncontained underwater explosion where interference between the primary pulse generated by the explosion and later pulses generated by the oscillating size of the gas bubble produce a regular pattern of modulations such as those observed from 171201.

A possible alternative explanation for the source of 171115 is that the signals were generated by an underwater implosion. The ARA San Juan, a Thyssen Nordseewerke TR-1700 class of diesel-electric submarine, was designed to operate at water depths of up to 271 m (890 feet) (Cragg 1991). Given that the water depth in the region where the submarine wreck was located is around 900 m, it is therefore possible that the submarine imploded. It has been demonstrated that imploding a glass sphere in the water can generate high-frequency acoustic signals and bubble pulses (Ulrick 1963; Harben & Boro 2001; Blackman *et al.* 2004). Other experiments on underwater implosions have been carried out using cylinders manufactured out of either aluminium or steel. For example, Price & Shuler (1974) conducted an implosion experiment using steel cylindrical tanks that were either dropped or lowered into the ocean. The energy spectra of signals produced by the implosions, unlike those produced from either imploding glass spheres or underwater explosions, did not have a regular pattern of modulations. Similar results were obtained during experiments to record acoustic signals from underwater implosions of cylinders made out of ductile materials
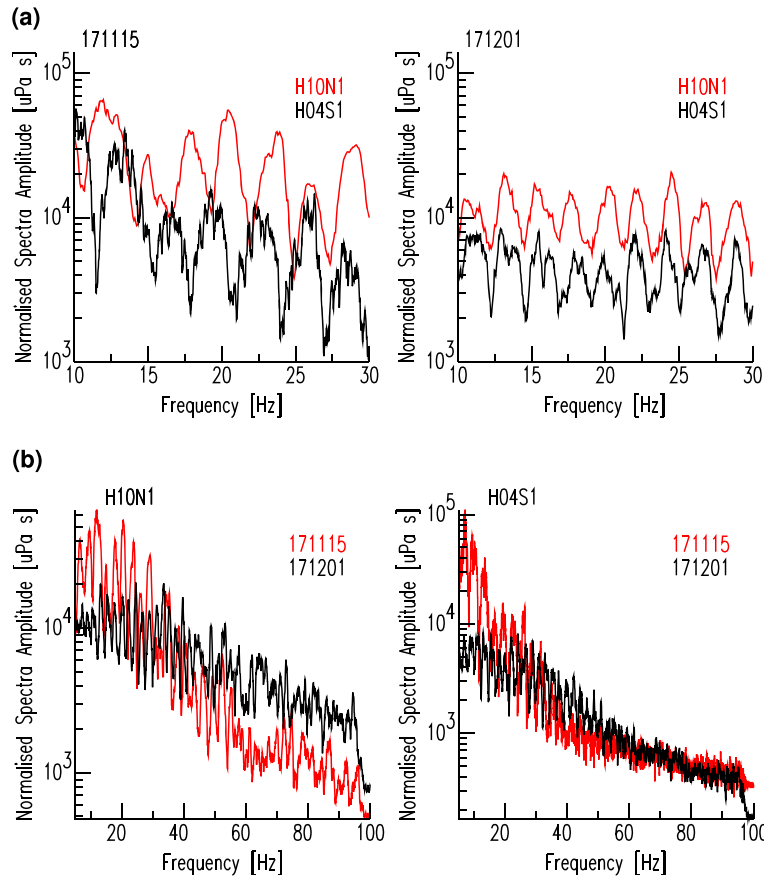
Figure 7. (a) Normalized smoothed amplitude spectra recorded at H10N1 and H04S1 for 171115 and 171201. The amplitude spectra of the signals were calculated using a 15 s time window at H10N1 and a 35 s time window at H04S1. (b) Comparison of normalized smoothed amplitude spectra recorded at H10N1 and H04S1 for 171115 and 171201.
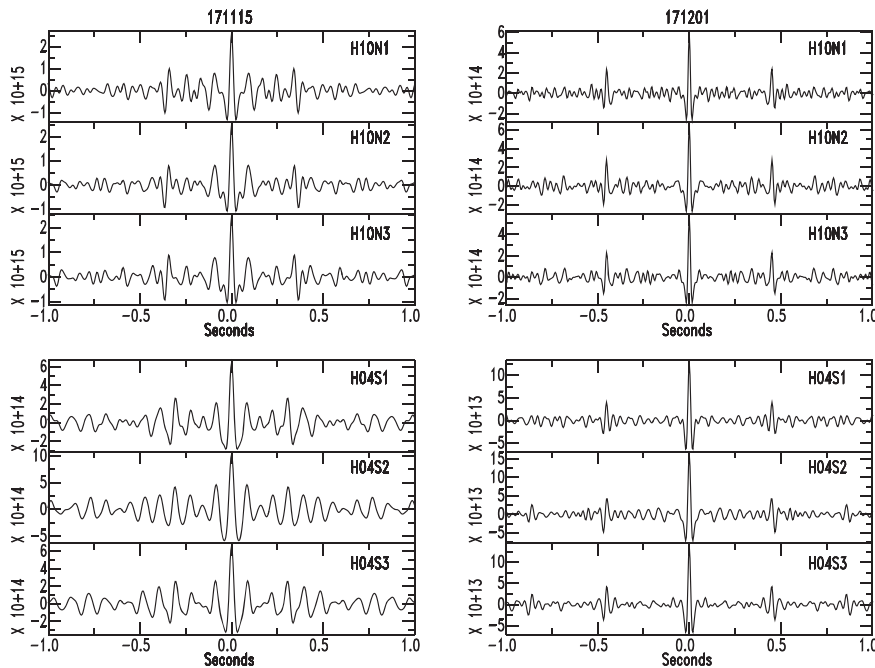

Figure 8. Autocorrelation traces at hydrophone sensors from the H10 and H04 hydrophone stations for 171115 and 171201 calculated for the 8–64 Hz passband.

conducted both in the laboratory (Turner 2004) and in an open-ocean environment (Dingus 2007). These experiments therefore suggest that a single implosion would not generate the differences in modulations in the amplitude spectra observed at H10N1 and H10S1 from 171115. The features observed in the spectra recorded for 171115 therefore suggest a more complex source than either a simple implosion or un-contained explosion. An intriguing explanation suggested by Vergoz *et al.* (2019) is that the modulations observed from 171115 are the result of two implosions with the frequency differences between the modulations at H10N1 and H04S1 a result of the two implosions being separated in space.

7 DATA AND RESOURCES

Data used in this study were recorded by the IMS and the GSN. The IMS data were obtained from the CTBTO in Vienna, Austria and are available to scientists and researchers from the CTBTO's virtual Data Exploitation Centre. The GSN is a co-operative scientific facility operated jointly by the IRIS, the United States Geological Survey (USGS) and the Seismological Facilities for the Advancement of Geoscience (SAGE) Award of the National Science Foundation (NSF), under Cooperative Support Agreement EAR-1851048. The facilities of IRIS Data Services, and specifically the IRIS Data Management Center, were used for access to GSN waveforms and related metadata used in this study. Figures in this study were made using the Generic Mapping Tools Software (Wessel & Smith 1998). The views expressed in this study are those of the authors and do not necessarily reflect those of the Preparatory Commission for the CTBTO.

REFERENCES

Antonov, J.I. *et al.*, 2010. World Ocean Atlas 2009, Volume 2: Salinity, NOAA Atlas NESDIS 66, U.S. Government Printing Office, Washington, DC, 184.

Baumgardt, D.R. & Der, Z., 1998. Identification of presumed shallow underwater chemical explosions using land-based regional arrays, *Bull. seism. Soc. Am.,* **88**(2), 581–595.

Blackman, D.K., de Groot-Hedlin, C., Harben, P.E., Sauter, A. & Orcutt, J.A., 2004. Testing low/very low frequency acoustic sources for basin-wide propagation in the Indian Ocean, *J. acoust. Soc. Am.,* **116,** 2057–2066.

Bóndar, I., Myers, S.C., Engdahl, E. & Bergmann, E.A., 2004. Epicentre accuracy based on seismic network criteria, *Geophys. J. Int.,* **156,** 483–496.

Bowers, D. & Selby, N.D., 2009. Forensic seismology and the Comprehensive Nuclear-Test-Ban Treaty, *Annu. Rev. Earth Planet. Sci.,* **37,** 209–236.

Bratt, S.R. & Bache, T.C., 1988. Locating events with a sparse network of regional arrays, *Bull. seism. Soc. Am.,* **78,** 1773–1795.

British Broadcasting Corporation, 2017. 'Argentina missing submarine: loud noise investigated'. Available at: https://www.bbc.co.uk/news/world-latin-america-42092897, Accessed June 2020.

Chapman, N.R., 1985. Measurement of the waveform parameters of shallow explosive charges, *J. acoust. Soc. Am.,* **78,** 672–681.

Comprehensive Nuclear-Test-Ban Treaty Organisation(CTBTO), 2017. 'Media advisory - CTBTO hydroacoustic data to aid in search for missing sub San Juan'. Available at: https://www.ctbto.org/press-centre/media-advisories/2017/media-advisory-ctbto-hydroacoustic-data-to-aid-in-search-for-missing-sub-san-juan/, Accessed June 2020.

Cragg, C.H., 1991. The United States versus the third world submarine: are we ready?, Report No. AD-A236 872, Naval War College, Newport, RI.

Dall'Osto, D.R., 2019. Source triangulation utilizing three-dimensional arrivals: application to the search for the ARA San Juan submarine, *J. acoust. Soc. Am.,* **146,** 2104–2112.

De Groot-Hedlin, C., Blackman, D.K. & Scott Jenkins, C., 2009. Effects of variability associated with the Antarctic circumpolar current on sound propagation in the ocean, *Geophys. J. Int.,* **176,** 478–490.

Dingus, M., 2007. Pressure vessel implosion sea test—final report, SBIR phase II topic N01-106 final report, contract no. N00024-04-C-4145.

Evernden, J.F., 1969. Precision of epicenters obtained by small numbers of world wide stations, *Bull. seism. Soc. Am.,* **59,** 1365–1398.

Evers, L.G., Green, D.N., Young, N.W. & Snellen, M., 2013. Remote hydroacoustic sensing of large icebergs in the southern Indian Ocean: implications for iceberg monitoring, *Geophys. Res. Lett.,* **40,** 4694–4699.

Fetterer, F., Knowles, K., Meier, W.N., Savoie, M. & Windnagel, A.K., 2017. 2017 to present, updated daily Sea Ice Index, Version 3. National Snow and Ice Data Center, Boulder, Colorado, USA.

Gavrilov, A.N. & Mikhalevsky, P.N., 2006. Low-frequency acoustic propagation loss in the Arctic Ocean: results of the Arctic climate observations using underwater sound experiment, *J. acoust. Soc. Am.,* **119,** 3694–3706.

Green, D.N., 2017. A *P*-wave magnitude scale for the UK: initial results, AWE Report 63/17.

Hanson, J., Le Bras, R., Dysart, P., Brumbaugh, D., Gault, A. & Guern, J., 2001. Operational processing of hydroacoustics at the Prototype International Data Center, *Pure appl. geophys.,* **158,** 425–456.

Harben, P.E. & Boro, C.O., 2001. Implosion source development and Diego Garcia reflections, in *Proceedings of the 23rd Annual Seismic Research Review: Worldwide Monitoring of Nuclear Explosions,* Jackson Hole, Wyoming.

Heyburn, R., Nippress, S.E.J. & Bowers, D., 2018. Seismic and hydroacoustic observations from underwater explosions off the east coast of Florida, *Bull. seism. Soc. Am.,* **108**(6), 3612–3624.

Jacob, A.W.B. & Neilson, G., 1977. Magnitude determination on LOWNET, Institute of Geological Sciences, Global Seismology Research Group Report 86.

Jensen, F.B., Kuperman, W.A., Porter, M.B. & Schmidt, H., 2000. *Computational Ocean Acoustics,* Springer-Verlag, ch. 1.

Jordan, T.H. & Sverdrup, K.A., 1981. Teleseismic location techniques and their application to earthquakes in the South-Central Pacific, *Bull. seism. Soc. Am.,* **71,** 1105–1130.

Kennett, B.L.N., 1993. The distance dependence of regional phase discriminants, *Bull. seism. Soc. Am.,* **83,** 1155–1166.

Koper, K.D., Wallace, T.C., Taylor, S.R. & Hartse, H.E., 2001. Forensic seismology and the sinking of the Kursk, *EOS, Trans. Am. geophys. Un.,* **82**(4), 37–46.

Le Bras, R.J., Kuzma, H., Sucic, V. & Bokelmann, G., 2016. Observations and Bayesian location methodology of transient acoustic signals (likely blue whales) in the Indian Ocean, using a hydrophone triplet, *J. acoust. Soc. Am.,* **139**(5), 2656–2667.

Locarnini, R.A., Mishonov, A.V., Antonov, J.I., Boyer, T.P., Garcia, H.E., Baranova, O.K., Zweng, M.M. & Johnson, D.R., 2010. *World Ocean Atlas 2009, Volume 1: Temperature,* NOAA Atlas NESDIS 68, U.S. Government Printing Office, 184.

Maienschein, J.L., 2002. Estimating equivalency of explosives through a thermochemical approach, Lawrence Livermore National Lab. Report UCRL-JC-147683.

Metz, D., Watts, A.B., Grevemeyer, I. & Rodgers, M., 2018. Tracking submarine volcanic activity at Monowai: constraints from long-range hydroacoustic measurements, *J. geophys. Res.,* **123**(9), 7877–7895.

Myers, S.C. *et al.*, 2010. A crust and upper-mantle model of Eurasia and North Africa for Pn travel-time calculation, *Bull. seism. Soc. Am.,,* **100,** 640–656.

Nielsen, P.L. *et al.*, 2020. CTBTO's data and analysis pertaining to the search for the missing Argentine submarine ARA San Juan, *Pure. appl. Geophys.,* https://doi.org/10.1007/s00024-020-02445-9.

Nowlin, W.D. & Klinck, J.M., 1986. The physics of the Antarctic circumpolar current, *Rev. Geophys.,* **24**(3), 469–491.

Ocean Infinity, 2018. 'Ocean Infinity locates the missing Argentinian submarine, ARA San Juan'. Available at: https://oceaninfinity.com/2019/09/ocean-infinity-locates-the-missing-argentinian-submarine-ara-san-juan/, Accessed June 2020.

Okal, E.A., 2001. T-phase stations for the International Monitoring System of the Comprehensive Nuclear-Test Ban Treaty: a global perspective, *Seismol. Res. Lett.,* **72**(2), 186–195.

Porter, M.B. & Bucker, H.P., 1987. Gaussian beam tracing for computing acoustic fields, *J. acoust. Soc. Am.,* **82,** 1349–1359.

Price, S.R. & Shuler, V.K., 1974. Sounds from implosions of steel cylinders underwater, Naval Ordnance Laboratory Report No. NOLTR 74-168.

Prior, M.K., 2009. Improving the accuracy of in-water travel-time predictions for seismic event location using two-dimensional underwater acoustic propagation modelling, in *Proceedings of IACM UAM,* eds Papadakis, J.S. & Bjorno, L., pp. 997–1002, Nafplion, Greece.

Prior, M.K. & Brown, D.J., 2010. Estimation of depth and yield of underwater explosions from first and second bubble-oscillation periods, *IEEE J. Ocean. Eng.,* **35**(1), 103–112.

Savage, B. & Helmberger, D.V., 2001. Kursk explosion, *Bull. seism. Soc. Am.,,* **91**(4), 753–759.

Turner, S.E., 2004. Small-scale implosion testing of glass and aluminum cylinders, NUWC-NPT technical memorandum 04-061, Naval Undersea Warfare Center Division, Newport, RI.

Ulrick, R.J., 1963. Implosions as sources of underwater sound, *J. acoust. Soc. Am.,* **35,** 2026–2027.

United States Navy Department, 1947. *Ordnance Pamphlet 1664, United States Explosive Ordnance,* Navy Department, Bureau of Ordnance.

Vergoz, J., Cansi, Y., Cano, Y. & Gaillard, P., 2019. Analysis of hydroacoustic signals associated to the loss of the Argentinian ARA San Juan submarine, in *2019 CTBTO Science and Technology Conference*, Vienna, Austria.

Wessel, P. & Smith, W.H.F., 1998. New improved version of the Generic Mapping Tools released, *EOS, Trans. Am. geophys. Un.,* **79,** 579.